SBA-16-Mediated Nanoparticles Enabling Accelerated Kinetics in Cyclic Methane Conversion to Syngas at Low Temperatures

Yan Liu,[§] Lang Qin,*[,§] Jianhua Pan,[§] Yu-Yen Chen, Josh W. Goetze, Dikai Xu, Jonathan A. Fan, and Liang-Shih Fan*

Cite This: https://dx.doi.org/10.1021/acsaem.0c01495

Read Online

ACCESS | Metrics & More | Article Recommendations | Supporting Information

ABSTRACT: To meet the globally growing energy demands, it is essential to develop schemes with higher fuel conversion efficiency at temperatures <1000 °C while suppressing emissions of CO_2. Iron oxide nanoparticles supported by mesoporous silica SBA-16 (Fe_2O_3@SBA-16) is conceived and developed in this study for chemical looping partial oxidation, yielding syngas selectivity above 95% with operating temperatures as low as around 400 °C is achieved, a temperature that is 600 °C lower than the conventional operating temperature. The methane conversion rate for Fe_2O_3@SBA-16 is 52 and 660% higher than those for established nanoparticle oxygen carriers and bulk oxygen carriers, respectively. Dynamic Monte Carlo simulations are conducted that demonstrate the distinct effects of nanoparticle loading and particle size distribution on 3-D interconnected Fe_2O_3@SBA-16, affirming its accelerated reaction kinetics. This finding has significant implications in mesoporous materials and broadens research domains in other cyclic redox energy systems.

KEYWORDS: *chemical looping, oxygen carrier, nanoparticle, diffusivity, trapping and congestion effect*
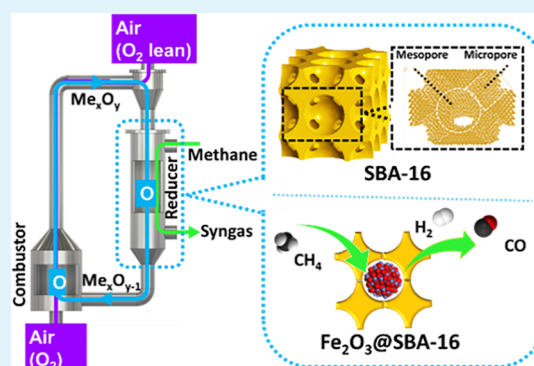
1. INTRODUCTION

The world's energy demands are expected to increase more than threefold over the next century. Hence, the energy industries acknowledge the necessity of seeking cost-efficient and environmentally friendly alternatives to crude oil. The continued discovery of shale gas and fire—ice reservoirs, together with the expanding renewable biogas production, manifests that methane is a promising alternative. Methane is the main feedstock for generating vital intermediate to fuels and value-added chemicals.[1,2] However, the high stability of C—H bonds, negligible electron affinity, and low polarizability of methane molecules (CH_4) require costly catalysts,[3] a high operating temperature, high steam consumption, and/or air separation in the industrial methane process, which is energy intensive and is associated with CO_2 emission control. Consequently, a cost-effective approach that can enhance energy efficiency and reduce carbon emissions, while promoting syngas selectivity and yield at lower temperatures, is desired.[4]

Chemical looping partial oxidation (CLPO) is an emerging approach that can alleviate the aforementioned methane transformation requirements. A viable CLPO process comprising of redox cycles[5−9] of metal oxide oxygen carriers in two interconnected reactors is illustrated in Figure 1. Specifically, in contrast to conventional fossil fuel reforming and utilization processes, CLPO features in direct production of high-quality
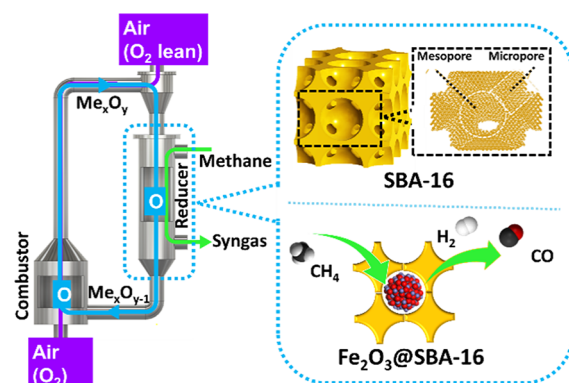

Figure 1. Chemical looping partial oxidation concept of mesoporous silica SBA-16 supported Fe_2O_3 oxygen carrier, Fe_2O_3@SBA-16.

syngas with minimal energy penalty and no requirement for an air separation unit, water—gas shift reactor, or CO_2 separation

unit. The lowest operating temperature achieved in the emerging nanomaterial-engaged CLPO process is 550 °C with syngas selectivity over 87%, using Ni-rABO_3 system oxygen carriers.[10] Higher operating temperatures generate visible carbon deposition in the Ni-rABO_3 system, which narrows the CLPO operating temperature window significantly. Consequently, it remains challenging and necessary to develop cost and energy efficient processes to concurrently achieve higher syngas selectivity above 90% and methane conversion at broader operating temperature windows with the lower limit below 550 °C and the higher limit below 1000 °C.

Mesoporous materials have been demonstrated as a versatile platform for applications in energy materials, chemistry, and medical science, including adsorption and catalysis,[11−15] chemical sensing,[16] drug delivery,[17,18] and separation technology.[19,20] Mesoporous silica possesses large surface areas and high thermal stability[21] with a controllable pore structure and pore size distribution. The adjustable structural features in mesoporous supports can facilitate diverse reactant mass transfer and can be tailored to enhance the efficiency of catalytic processes and reaction kinetics to a different extent. Considerable interest has been attracted by exploring nano-scaled redox systems in fuel conversion and utilization supported by mesoporous silica.[22] Nevertheless, a systematic understanding of pore structure-dependent diffusivity has not been established, which hinders the application of mesoporous silica in redox processes. Thus, success[23] in long-term nanoparticle stability and high reactivity can significantly benefit energy industries, such as photocatalysis and chemical looping processes.

Multiscale modeling has demonstrated that iron oxide nanoparticles exhibit a strong size effect that facilitates CO and H_2, instead of CO_2 and H_2O, formation and thus enhances syngas selectivity substantially.[23] In this context, we develop Fe_2O_3 nanoparticle oxygen carriers supported by mesoporous silica SBA-16 (Fe_2O_3@SBA-16), which not only exhibits a high syngas selectivity of 95% with high conversion rates but also can be operated at broad operating temperature windows between 400 and 800 °C with carbon inhibition capability (Figure 1). To gain a mechanistic insight in the high reactivity Fe_2O_3@SBA-16, another mesoporous supported oxygen carrier (Fe_2O_3@SBA-15) with almost identical pore size but different pore arrangement is also investigated. We discovered that the distinct structures enable significantly higher gas diffusivity in Fe_2O_3@SBA-16 compared to Fe_2O_3@SBA-15, which is confirmed by dynamic Monte Carlo simulations. Computational modeling reveals that the Fe_2O_3 nanoparticles influence gas diffusivity by different molecular mechanics in these two mesoporous structures with a different flow pattern. The gas molecules in Fe_2O_3@SBA-15 tend to be trapped by the nanoparticles located in the 2-D cylindrical channels, especially when the nanoparticle size maximize to the mesopore size. On the other hand, the 3-D interconnected pores of Fe_2O_3@SBA-16 facilitate the gas diffusion and decrease the trapping effect significantly. As a result, the diffusivity of Fe_2O_3@SBA-16 is less sensitive to the nanoparticle size and mainly depends on the nanoparticle loading. This study is expected to impact broadly on industrial applications of CLPO as well as other redox reaction systems, such as photocatalysis and chemical looping in fuel conversion and utilization.

2. EXPERIMENTAL SECTION

2.1. Sample Preparation. The sample was prepared by an impregnation method. $Fe(NO_3)_3 \cdot 9H_2O$ (3.03 g) was first dissolved in 4 mL of ethanol. Mesoporous support SBA-15 or SBA-16 (0.1 g) was then added in the solution and the whole was subject to ultrasonic treatment for 1 h. The suspension was mixed under vigorous stirring overnight. The solid precursor was collected by centrifugation and cleaned before drying in air to make sure no iron oxide will deposit on the surface of the support. The as-prepared precursor was calcined at 600 °C for 5 h to obtain the final product.

The weight loading of the Fe_2O_3 nanoparticles was measured in a thermogravimetric analysis (TGA) equipment. The sample (15 mg) was mounted in a Setaram TGA device and fully reduced by 50% H_2 (100 mL/min of H_2 balances with 100 mL/min He) under 800 °C. The oxygen carrying capacity and weight loading of Fe_2O_3 in Fe_2O_3@SBA-15 and Fe_2O_3@SBA-16 were calculated by

$$\text{oxygen carrying capacity} = \frac{\Delta m}{m} \times 100\%$$

$$\text{weight loading} = \frac{\text{oxygen carrying capacity}}{30\%} \times 100\%$$

where Δm is the weight change during the reduction, m is the total weight of the sample, and 30% is the weight percentage of oxygen in Fe_2O_3. The result showed that Fe_2O_3@SBA-15 has an oxygen carrying capacity of 8.1% and Fe_2O_3 weight loading of 27%. Fe_2O_3@SBA-16 has an oxygen carrying capacity of 5.4% and a weight loading of 18%. The Fe_2O_3 volume loading of both samples are also evaluated by

$$\text{volume loading} = \frac{\text{weight loading}/\rho_{Fe_2O_3}}{v} \times 100\%$$

where v is the pore volume of the mesoporous support, and the density of α-Fe_2O_3 ($\rho_{Fe_2O_3}$) is 5.24 g/cm^3. Based on our surface analysis result, v is measured as 0.66 and 0.48 cm^3/g in SBA-15 and SBA-16, respectively. The result confirms that both Fe_2O_3@SBA-15 and Fe_2O_3@SBA-16 have similar volume loading of Fe_2O_3 nanoparticles, which are 7.5 and 6.7%, respectively.

2.2. Sample Characterization and Measurement. *2.2.1. Impact of Micropores in Mesoporous SBA-15 Support.* To eliminate the effect of micropores (<2nm) on the reactivity of oxygen carriers, mesoporous support SBA-15 was subject to heat treatment at 1000 °C for 4 h[24,25] to remove the interconnected pores.[26] The as-prepared support is noted as SBA-15$_{nip}$ (SBA-15 with no interconnected pores). Fe_2O_3@SBA-15$_{nip}$ was also synthesized and compared with Fe_2O_3@SBA-15. Both Fe_2O_3@SBA-15$_{nip}$ and Fe_2O_3@SBA-15 have identical reactivity, indicating the impact of the interconnected pores is negligible.

2.2.2. Surface Analysis. N_2 physisorption was used to analyze the solid surface and pore size distribution by a NOVA 4200 surface area analyzer. The surface areas were calculated adopting the Brunauer−Emmett−Teller (BET) method. Pore size distributions were calculated by the Brunauer−Joyner−Halenda (BJH) method based on the adsorption of the N_2 isotherm curve.

2.2.3. Transmission Electron Microscopy (TEM). TEM images were obtained on an FEI Tecnai G2 30 with a working voltage of 200 kV. A high-resolution TEM operation was performed on an FEI image-corrected Titan3 G2 60-300 S/TEM with a working voltage of 300 kV. The TEM images for fresh and reacted Fe_2O_3@SBA-15 after 100 redox cycles are shown in Figure S4. The TEM images of support SBA-15 and SBA-16 are shown in Figures S5 and S6.

2.2.4. TPR Analysis and Redox Reactions. The temperature-programmed reaction with methane was conducted in a Setaram thermogravimetric analysis (TGA) device. In each test, 20 mg of the sample was heated from 370 to 430°C and 650—850 °C with a heating ramp rate of 20 °C/min. The reducing gas is composed of 20 mL/min of CH_4 balanced with 180 mL/min of He. Mass spectrometry (MS) was used to analyze the outlet gas composition. The result of TPR for Fe_2O_3@SBA-15 is shown in Figure S4C,D.

The reaction rate and stability of the samples were tested in TGA with 100 reduction−oxidation (redox) cycles at 800 °C. In a reduction step, each sample reacted with 40 mL/min of CH_4 balanced with 100 mL/min of N_2 and 50 mL/min of He carrier gas for 5 min. In a regeneration step, each sample was oxidized by 100 mL/min of air balanced with 100 mL/min of N_2 for 5 min. A buffering step between reduction and regeneration was also performed with 100 mL/min of N_2 as the flushing gas to prevent the mixing of air and methane. The conversion rate of the oxygen carrier is calculated by

$$\text{conversion rate} = \frac{\Delta m}{m_{Fe_2O_3} \times 30\%}$$

where Δm is the weight change during oxidation, $m_{Fe_2O_3}$ is the weight of Fe_2O_3 in the total sample, and 30% is the weight percentage of oxygen in Fe_2O_3. Figure S5 showed the conversion rate of 100 redox cycles at 800 °C.

For better comparison, gas concentrations and the dTG value are divided by the total mass of available oxygen in the sample; thus, the unit of the gas concentration is "%/g_O". The equation is shown below:

$$\text{concentration} = \frac{x_i}{m_{Fe_2O_3} \times 30\%}$$

where x_i stands for the gas mole fraction, $m_{Fe_2O_3}$ is the weight of Fe_2O_3 in the total sample, and 30% is the weight percentage of oxygen in Fe_2O_3. The selectivity is calculated by

$$\text{selectivity} = \frac{c_{CO}}{c_{CO} + c_{CO_2}} \times 100\%$$

where c_{CO} is the mole fraction of the CO product, and c_{CO_2} is the mole fraction of the CO_2 product.

2.3. Grand Canonical Monte Carlo (GCMC) Simulation. The loading of methane molecules in SBA-15 and SBA-16 under experimental conditions were modeled by GCMC, i.e., constant μVT simulations with open-source software LAMMPS.[27]

The single units of SBA-15 and SBA-16 frameworks were determined to be 100.24 Å × 171.84 Å × 100.24 Å and 100.24 Å × 100.24 Å × 100.24 Å β-cristobalite crystalline matrices, respectively. The mesopore diameter of SBA-15 is 80 Å and no micropore was considered. The mesopore and interconnected micropore diameters of SBA-16 were 60 Å and 40 Å, respectively.

In the established units of SBA-15 and SBA-16, all silicon atoms with less than four bonds were removed and the oxygen atoms connected to single silicon were saturated by adding an extra hydrogen atom. The frameworks were first minimized and then set to be fixed in GCMC simulations. The Hill-Saucer force field[28,29] was used to model the framework−framework interactions. DREIDING FF[30] was used to model the methane−methane and methane−framework interactions. For the Hill-Saucer FF, the potential between atoms is defined as

$$E = E(\text{bonds}) + E(\text{angles}) + E(\text{torsions}) + E(\text{bond} - \text{bond})$$
$$+ E(\text{angle} - \text{angle}) + E(\text{bond} - \text{angle})$$
$$+ E(\text{angle} - \text{angle} - \text{torsion}) + E(\text{nonbond})$$

$$E(\text{bonds}) = \sum_{\text{bonds}} [K_2(b - b_0)^2 + K_3(b - b_0)^3 + K_4(b - b_0)^4]$$

$$E(\text{angles}) = \sum_{\text{angles}} [H_2(\theta - \theta_0)^2 + H_3(\theta - \theta_0)^3 + H_4(\theta - \theta_0)^4]$$

$$E(\text{torsions}) = \sum_{\text{torsions}} [V_1(1 - \cos\phi) + V_2(1 - \cos 2\phi) + V_3(1 - \cos 3\phi)]$$

$$E(\text{bond} - \text{bond}) = \sum_b \sum_{b'} F_{bb'}(b - b_0)(b' - b_0')$$

$$E(\text{angle} - \text{angle}) = \sum_\theta \sum_{\theta'} F_{\theta\theta'}(\theta - \theta_0)(\theta' - \theta_0')$$

$$E(\text{bond} - \text{angle}) = \sum_b \sum_\theta F_{b\theta}(b - b_0)(\theta - \theta_0)$$

$$E(\text{angle} - \text{angle} - \text{torsion})$$
$$= \sum_\theta \sum_{\theta'} \sum_\phi K_{\theta\theta'\phi}\cos\phi(\theta - \theta_0)(\theta' - \theta_0')$$

$$E(\text{nonbond}) = \sum_{i>j} \frac{q_i q_j}{\epsilon r_{ij}} + \frac{A_{ij}}{r_{ij}^9} + \frac{B_{ij}}{r_{ij}^6}$$

where b, θ, and ϕ are bond lengths, bond angles, and torsional angles, respectively; r_{ij} is the distance between two atoms, q_j is the charge, and ϵ is the dielectric constant and is set to be 1.0. All the constants for the Hill-Saucer FF are listed in Table S1, where O_{sh} denotes the oxygen atoms connecting with one silicon and one hydrogen atoms, and O_{ss} denotes the oxygen atoms connecting with two silicon atoms. Also, the charges for each atom are accumulated by

$$q_i = \sum_{j=1}^{\text{bond on } i} \delta_{ij}$$

As for the DREIDING FF used to model the methane−methane and methane−framework interactions, the potential is defined by

$$E = E(\text{bonds}) + E(\text{angles}) + E(\text{nonbond})$$
$$= \sum_{\text{bonds}} K_2(b - b_0)^2 + \sum_{\text{angles}} H_2(\theta - \theta_0)^2 + \sum_{i>j} \frac{q_i q_j}{\epsilon r_{ij}}$$
$$+ 4\epsilon_{ij}\left(\left(\frac{\sigma_{ij}}{r_{ij}}\right)^{12} - \left(\frac{\sigma_{ij}}{r_{ij}}\right)^6\right)$$

The parameters are shown in Table S2, where the subscript "m" stands for methane.

A cutoff radius of 10.5×10^{-10} m was used for the nonbond L−J force, and Ewald summation was applied in the calculation of long-range columbic force.

2.4. Dynamic Monte Carlo Simulations of Methane in Fe_2O_3@SBA-15 and Fe_2O_3@SBA-16. Dynamic Monte Carlo (DMC) simulations have been widely used to study the Knudsen diffusion in porous materials.[31,32] In this work, a computational domain consisting of interconnected porous networks and loading with nanoparticles was used to model the methane diffusion in Fe_2O_3@SBA-15 and Fe_2O_3@SBA-16. Periodic boundary conditions were applied in all three directions; the methane−methane collisions were neglected, and methane molecules were represented by material points with velocities. The simulations can be summarized as the following few steps.

At the starting point of simulations, randomly generated methane molecules were placed inside the porous volume and were given randomly selected velocity directions.

The methane molecules moved forward until colliding with the wall of the porous network, either with the surface of the placed-in nanoparticles or with the surface of SBA-15 or SBA-16.

After collision, methane molecules were bounce back, and new directions were randomly selected according to the cosine law.[33]

Recur to step 2.

After sufficient collisions, the self-diffusivity was estimated by the Einstein's equation:

$$D = \lim_{t\to\infty} \frac{1}{\alpha t} |\vec{l}(t) - \vec{l}(0)|^2 = \lim_{t\to\infty} \frac{v_{ave}}{\alpha L} |\vec{l}(t) - \vec{l}(0)|^2$$

where $\alpha = 6$ for 3-D simulations, L is the total trajectory length of the methane molecules, and v_{ave} is the average gas velocity of methane by
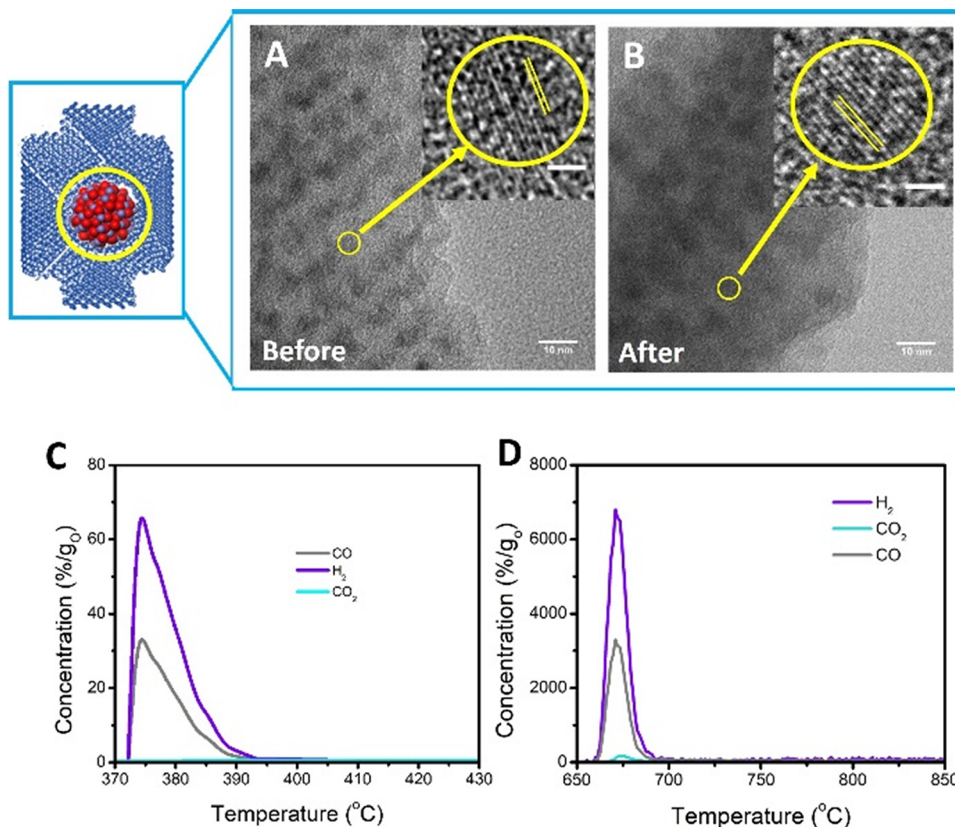
Figure 2. Experimental results for Fe_2O_3@SBA-16. (A) TEM image of fresh Fe_2O_3@SBA-16. (B) TEM image of Fe_2O_3@SBA-16 after 100 redox cycles (inset scale 1 nm). (C) TPR result of Fe_2O_3@SBA-16 at 370−430 °C. (D) TPR result of Fe_2O_3@SBA-16 at 650−850 °C.

$$v_{ave} = \sqrt{\frac{8RT}{\pi M}}$$

and M is the mass per mole of methane.

If the diffusion process is highly heterogeneous, e.g., in the nanochannels of SBA-15, component-wise diffusivity can be expressed as

$$D_i = \lim_{t \to \infty} \frac{1}{\alpha t} |l_i(t) - l_i(0)|^2 = \lim_{t \to \infty} \frac{v_{ave}}{2L} |l_i(t) - l_i(0)|^2$$

where $i = x$, y or z.

The nanoparticles were randomly placed in the mesopores of the porous network without overlapping with each other. Large enough computational domains was considered to eliminate the fluctuations due to the randomness of nanoparticle positions. For SBA-15, two periodic nanochannels, each with a length of 10,240,000 nm and a diameter of 8 nm, were considered. For SBA-16, a periodic domain of 1024 nm × 1024 nm × 1024 nm was considered with the meso- and micropore diameters being 6 and 4 nm, respectively.

3. RESULTS AND DISCUSSION

3.1. The Impact of Size Effect in Fe_2O_3@SBA-16. The structural features of freshly synthesized Fe_2O_3@SBA-16 are presented in Figure 2, with Fe_2O_3 nanoparticles of 3−6 nm dispersed in a highly ordered 3-D cubic structure. The Fe_2O_3 nanoparticles are single crystalline (Figure 2 inset) with sphere-like structures. The surface area of Fe_2O_3@SBA-16 was confirmed as 346 m^2/g by using BET analysis. No agglomeration of nanoparticles was observed on the surface of Fe_2O_3@SBA-16, suggesting that all the nanoparticles are embedded in the mesopores, following the mesoporous support profile. The particle size remains unchanged with no

sign of sintering after 100 redox cycles as shown in Figure 2, confirming the high stability of Fe_2O_3@SBA-16.

The temperature programmed reduction (TPR) study with methane was carried out on Fe_2O_3@SBA-16 with an oxygen carrying capacity of 5.4%, and the results are shown in Figure 2C,D. This is the optimal nanoparticle loading with minimal surface agglomeration. Both lower temperatures (370−430 °C) and higher temperatures (650−850 °C) were applied to test the reactivity of Fe_2O_3@SBA-16 in broad temperature windows (Figure 2). The onset reaction temperature was as low as around 400 °C in Fe_2O_3@SBA-16, which is 600 °C lower than bulk Fe_2O_3[1] and 150 °C lower than the Ni-rABO$_3$ system[10] oxygen carriers. Significantly increased reactivity is observed at higher temperatures due to the higher kinetic energy of molecules. The overall selectivity to syngas for Fe_2O_3@SBA-16 is higher than 95%, exceeding the maximum value of 87% that other transition metal oxide systems[10] can achieve. The high selectivity is induced by the size effect of the Fe_2O_3 nanoparticle oxygen carriers that substantially promote syngas formation. Mechanistically, Fe_2O_3 nanoparticles less than 8 nm facilitate CH_4 adsorption and activation due to an upward shift of the Fe d-band, while promoting the Fe−O bond cleavage and CO and H_2 over CO_2 and H_2O formation in methane conversion.[23] In this work, the nanoparticle sizes in Fe_2O_3@SBA-16 are in the range of 3−6 nm. Consequently, methane conversion kinetics is significantly promoted in Fe_2O_3@SBA-16. A ratio of H_2:CO at 2:1 indicates no carbon deposition during the TPR test.

In order to mimic the harsh environment in CLPO, the reactivity and stability of Fe_2O_3@SBA-16 was tested at an elevated temperature of 800 °C for 100 redox cycles. Figure 3
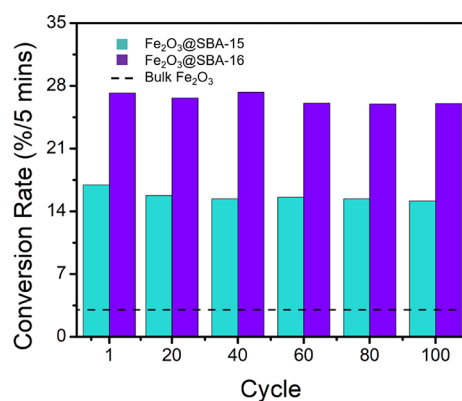
Figure 3. Redox cycle results of Fe$_2$O$_3$@SBA-16 compared with Fe$_2$O$_3$@SBA-15 and bulk Fe$_2$O$_3$.

shows the conversion rates of Fe$_2$O$_3$@SBA-16 during the 1st, 20th, 40th, 60th, 80th, and 100th cycle. As comparison, we also tested Fe$_2$O$_3$@SBA-15 with a surface area of 436m^2/g and particle size of 5−8nm. The average conversion rate for Fe$_2$O$_3$@SBA-16 is 26% in 5 min, which is 52 and 660% higher than Fe$_2$O$_3$@SBA-15 and bulk Fe$_2$O$_3$,[1,34] respectively. Minimal fluctuation in conversion rates during 100 continuous cycles (Figure S4) indicates high chemical and physical stability in Fe$_2$O$_3$@SBA-16. No carbon deposition has been observed at the elevated temperature of 800 °C, suggesting Fe$_2$O$_3$@SBA-16 has higher carbon inhibition capability than perovskite nanomaterials.

3.2. Visualization of Diffusion Modeling. Due to the similar pore size and surface area in Fe$_2$O$_3$@SBA-15 and Fe$_2$O$_3$@SBA-16, one can expect identical intrinsic kinetics dominated by the size effects.[23] Hence, the much higher conversion rate in Fe$_2$O$_3$@SBA-16 is believed to relate to structure-dependent gaseous diffusion. Grand canonical Monte Carlo (GCMC) simulations along with dynamic Monte Carlo (DMC) simulations[31] were conducted in this study, with the computational details given in the Supporting Information. The model configurations of SBA-15 and SBA-16 frameworks are shown in Figure 4, where the geometrical parameters are consistent with the experimental results. Since the pore diameters are much smaller than the mean free path of the methane molecules, Knudsen diffusion of methane is considered as the dominating transport mechanism in both SBA-15 and SBA-16. This is confirmed by the GCMC

simulations in the range of temperature from 600 to 800 °C, where the calculated low methane loadings in SBA-15 (7−9 CH$_4$ molecules/unit cell) and SBA-16 (4−5 CH$_4$ molecules/unit cell) indicate that CH$_4$-surface collisions is much more frequent than the intermolecular collisions.

DMC simulations discover varying morphological effects of the Fe$_2$O$_3$ nanoparticles supported by different mesoporous networks on the CH$_4$ diffusivity (D_{CH_4}). Figure 5 features the
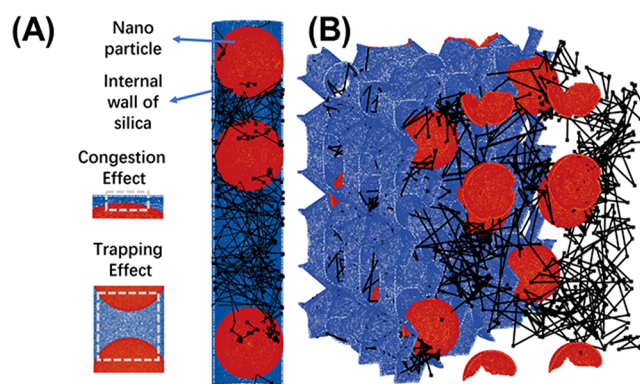

Figure 5. Illustration of trajectories of methane in DMC simulations for (A) Fe$_2$O$_3$@SBA-15 and (B) Fe$_2$O$_3$@SBA-16.

mesoporous networks of Fe$_2$O$_3$@SBA-15 and Fe$_2$O$_3$@SBA-16 adopted in the DMC simulations, and Figure 6 illustrates the influence of nanoparticle size and loading on D_{CH_4}. As shown in Figure 6, DMC simulations reveal that the dependence of D_{CH_4} on nanoparticle size is distinct between Fe$_2$O$_3$@SBA-15 and Fe$_2$O$_3$@SBA-16. D_{CH_4} of Fe$_2$O$_3$@SBA-15 ($D_{CH_4, Fe_2O_3 @ SBA-15}$) decreases significantly with increasing nanoparticle sizes, whereas D_{CH_4} of Fe$_2$O$_3$@SBA-16 ($D_{CH_4, Fe_2O_3 @ SBA-16}$) is nearly independent of nanoparticle size. A critical relative diameter between nanoparticles and mesopore ($d_r^{critical}$) is established to determine $D_{CH_4, Fe_2O_3 @ SBA-15}$ and $D_{CH_4, Fe_2O_3 @ SBA-16}$ under different particle loadings. $D_{CH_4, Fe_2O_3 @ SBA-16}$ is higher than $D_{CH_4, Fe_2O_3 @ SBA-15}$ in the region above $d_r^{critical}$, whereas $D_{CH_4, Fe_2O_3 @ SBA-16}$ is lower than $D_{CH_4, Fe_2O_3 @ SBA-15}$ in the region below $d_r^{critical}$. The $d_r^{critical}$ is between 0.93 and 0.95 in this simulation when the nanoparticle loading is 0.10 and 0.04,
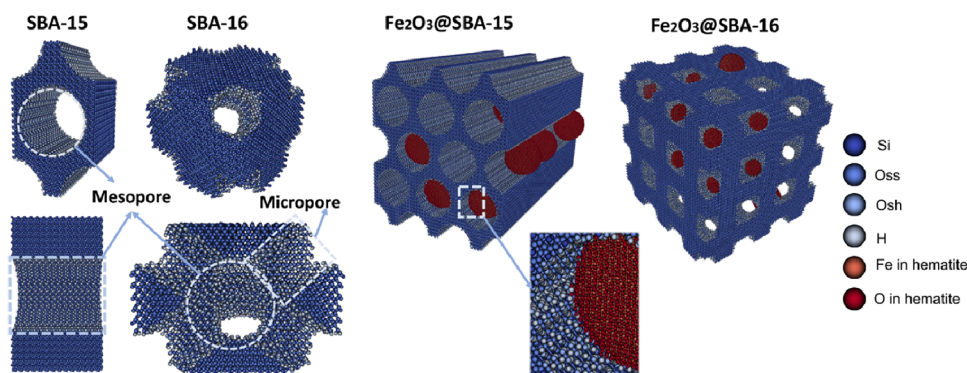

Figure 4. Unit cells and porous networks of SBA-15 and SBA-16. From left to right: unit cell for SBA-15, unit cell for SBA-16, porous network for SBA-15, and porous network for SBA-16. O$_{ss}$ denotes oxygen atoms connecting with two silicon atoms; O$_{sh}$ denotes oxygen atoms in the surface of −OH.
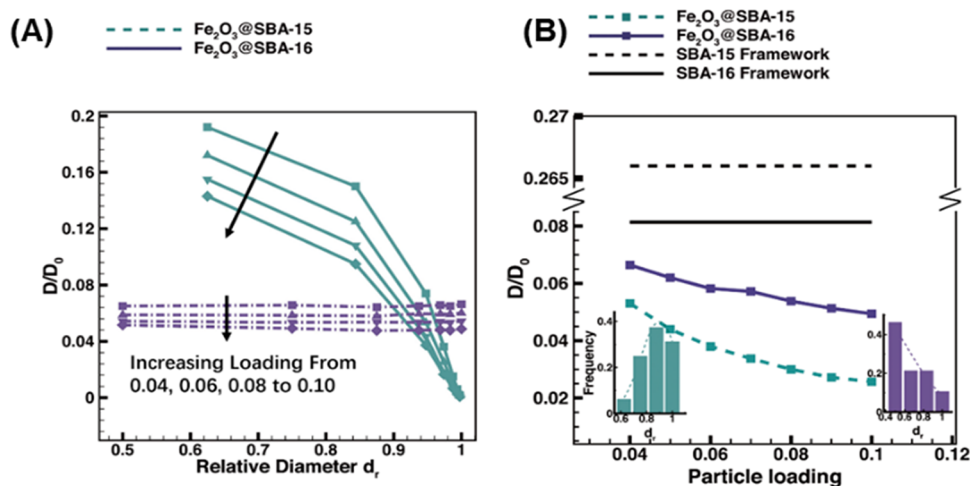
Figure 6. Diffusivity of Fe_2O_3@SBA-15 and Fe_2O_3@SBA-16. $D_0 = v_{ave}l_{unitcell}$, where v_{ave} is the average gas velocity and $l_{unitcell}$ = 10.24 nm, $d_r = \frac{d_{nanoparticle}}{d_{mesopore}}$. (A) Diffusivity results with uniform particle size. (B) Diffusivity results with varying particle sizes obeying the cutoff normal distribution in section [5 nm, 7.98nm] for SBA-15 and [3nm, 6nm] for SBA-16.

respectively, indicating a high d_r facilitates methane diffusion in Fe_2O_3@SBA-16.

Here, we discover two distinct factors that have a significant impact on methane diffusivity. The congestion effect is defined as the phenomena that confines methane molecule diffusion in the space between Fe_2O_3 nanoparticles and the internal surface of the silica wall. The trapping effect is defined as the phenomena that methane molecules are caged in the space created by neighboring Fe_2O_3 nanoparticles. Both effects are illustrated in Figure 6. The very different sensitivity of D_{CH_4} with respect to nanoparticle size between Fe_2O_3@SBA-15 and Fe_2O_3@SBA-16 can be attributed to their distinct flow patterns, which are dictated by the morphology of the mesoporous networks shown in Figures 5 and 6. For Fe_2O_3@SBA-15, the mesopores are constructed by 2-D cylindrical channels; as a result, methane molecules would be trapped in the spaces between neighboring nanoparticles by the narrow spaces between the nanoparticle and the silica wall when the nanoparticle size becomes considerable, as shown in Figure 5. On the other hand, mesopores in Fe_2O_3@SBA-16 adopts a fully connected 3-D body-centered cubic structure, which substantially mitigates the trapping effect with a minimal congestion effect by allowing the molecules to bypass through the micropores that surround the mesopore cavity, as shown in Figure 5. Therefore, $D_{CH_4, Fe_2O_3 @ SBA - 15}$ is found much higher than $D_{CH_4, Fe_2O_3 @ SBA - 15}$ when the relative diameter is above $d_r^{critical}$, as presented in Figure 6. Figure 6 further considers the cases where the size of dispersed nanoparticles follows the cutoff normal distribution, which matches the experimental observations from TEM and redox performance in the current study. It is also worth pointing out that $D_{CH_4, Fe_2O_3 @ SBA - 15}$ is higher than $D_{CH_4, Fe_2O_3 @ SBA - 16}$ when the relative diameter is below $d_r^{critical}$, as indicated in Figure 6. This can be explained by the fact that CH_4 diffuses faster in the framework of SBA-15 than SBA-16 without the presence of nanoparticles as shown in Figure 6. Thus, when the loading particles possess small sizes, the congestion effect and trapping effect in the SBA-15 framework can be overcome. The nanoparticle trapping effect is also reflected by the results in Figure 6 that a higher loading

leads to a lower D_{CH_4} in both mesoporous networks. In short, the DMC results demonstrate the necessity of considering the trapping effect and congestion effect of nanoparticles and mesoporous structures on diffusivity, and the insights derived from this study are of great importance to the optimization of the reactive performance of future mesoporous supported materials.

4. CONCLUSIONS

This study demonstrates that Fe_2O_3@SBA-16 exhibits high syngas selectivity of 95% in chemical looping methane partial oxidation. The effective temperature for syngas generation has a broad window of 400 and 800 °C in Fe_2O_3@SBA-16, which can sustain a variety of harsh environments in CLPO. This study opens up the path for nanoscaled oxygen carriers that can exhibit minimal high-temperature reactivity deterioration and adapt to broader operating temperature windows for chemical looping technology. While the intrinsic reaction kinetics for Fe_2O_3@SBA-16 is identical to other mesoporous oxygen carriers and is dominated by the nanoparticle size effect, its conversion rate is 60 and 660% higher than Fe_2O_3@SBA-16 and bulk Fe_2O_3, respectively. The DMC simulation confirms that the significant enhancement in the Fe_2O_3@SBA-16 conversion rate is highly related to its mesoporous structure and pore configuration. Specifically, the 3-D interconnected pore structure of SBA-16 exhibits a minimum variation of gas diffusivity versus nanoparticle size under a fixed Fe_2O_3 nanoparticle loading, whereas the 2-D cylindrical structure in other supports such as SBA-15 exhibits the nanoparticle size-sensitive diffusivity. Consequently, the reactivity is much higher in Fe_2O_3@SBA-16 compared with Fe_2O_3@SBA-15 over a wide range of operating temperatures. This work elucidates the relationship between mesopore structures and gas diffusivity in the CLPO methane conversion. It can provide new perspectives on redox material synthesis in chemical looping technology innovation.

■ ASSOCIATED CONTENT

ⓈⅠ Supporting Information

The Supporting Information is available free of charge at https://pubs.acs.org/doi/10.1021/acsaem.0c01495.

Surface analysis results of SBA-15 and SBA-16; surface analysis results of Fe_2O_3@SBA-15 and Fe_2O_3@SBA-16; surface analysis results of Fe_2O_3@SBA-15 and Fe_2O_3@SBA-16 after 100 redox cycles at 800 °C; TEM and TPR results of Fe_2O_3@SBA-15; TEM images of SBA-15 and SBA-16; Fe_2O_3 nanoparticle fast Fourier transform (FFT) patterns; conversion rate of oxygen carriers with CH_4; Hill-Sauer FF parameters; DREIDING FF parameters (PDF)

■ AUTHOR INFORMATION

Corresponding Authors

Lang Qin − Department of Chemical and Biomolecular Engineering, The Ohio State University, Columbus, Ohio 43210, United States of America; ⓞ orcid.org/0000-0002-2075-6505; Email: qin.96@osu.edu

Liang-Shih Fan − Department of Chemical and Biomolecular Engineering, The Ohio State University, Columbus, Ohio 43210, United States of America; Email: fan.1@osu.edu

Authors

Yan Liu − Department of Chemical and Biomolecular Engineering, The Ohio State University, Columbus, Ohio 43210, United States of America; ⓞ orcid.org/0000-0002-3459-6776

Jianhua Pan − Department of Chemical and Biomolecular Engineering, The Ohio State University, Columbus, Ohio 43210, United States of America; ⓞ orcid.org/0000-0002-2277-3157

Yu-Yen Chen − Department of Chemical and Biomolecular Engineering, The Ohio State University, Columbus, Ohio 43210, United States of America

Josh W. Goetze − Department of Chemical and Biomolecular Engineering, The Ohio State University, Columbus, Ohio 43210, United States of America

Dikai Xu − Department of Chemical and Biomolecular Engineering, The Ohio State University, Columbus, Ohio 43210, United States of America

Jonathan A. Fan − Department of Electrical Engineering, Ginzton Laboratory, Spilker Engineering and Applied Sciences, Stanford University, Stanford, California 94305, United States of America

Complete contact information is available at:
https://pubs.acs.org/10.1021/acsaem.0c01495

Author Contributions

§These authors contributed equally. The manuscript was written through contributions of all authors. All authors have given approval to the final version of the manuscript.

Notes

The authors declare no competing financial interest.

■ ACKNOWLEDGMENTS

■ REFERENCES

(1) Qin, L.; Guo, M.; Liu, Y.; Cheng, Z.; Fan, J. A.; Fan, L.-S. Enhanced methane conversion in chemical looping partial oxidation systems using a copper doping modification. *Appl. Catal., B* **2018**, *235*, 143−149.

(2) McFarland, E. Chemistry. Unconventional chemistry for unconventional natural gas. *Science* **2012**, *338*, 340−342.

(3) Goodman, E. D.; Latimer, A. A.; Yang, A.-C.; Wu, L.; Tahsini, N.; Abild-Pedersen, F.; Cargnello, M. Low-Temperature Methane Partial Oxidation to Syngas with Modular Nanocrystal Catalysts. *ACS Appl. Nano Mater.* **2018**, *1*, 5258−5267.

(4) Ravi, M.; Ranocchiari, M.; van Bokhoven, J. A. The direct catalytic oxidation of methane to methanol—A critical assessment. *Angew. Chem., Int. Ed.* **2017**, *56*, 16464−16483.

(5) Fan, L. *Chemical looping partial oxidation: gasification, reforming, and chemical syntheses*; Cambridge University Press: 2017

(6) Chung, C.; Qin, L.; Shah, V.; Fan, L.-S. Chemically and physically robust, commercially-viable iron-based composite oxygen carriers sustainable over 3000 redox cycles at high temperatures for chemical looping applications. *Energy Environ. Sci.* **2017**, *10*, 2318−2323.

(7) Chen, S.; Zeng, L.; Tian, H.; Li, X.; Gong, J. Enhanced lattice oxygen reactivity over Ni-modified WO_3-based redox catalysts for chemical looping partial oxidation of methane. *ACS Catal.* **2017**, *7*, 3548−3559.

(8) Liu, R.; Pei, C.; Zhang, X.; Chen, S.; Li, H.; Zeng, L.; Mu, R.; Gong, J. Chemical looping partial oxidation over $FeWO_x/SiO_2$ catalysts. *Chin. J. Catal.* **2020**, *41*, 1140−1151.

(9) Zhang, X.; Pei, C.; Chang, X.; Chen, S.; Liu, R.; Zhao, Z.-J.; Mu, R.; Gong, J. FeO_6 Octahedral Distortion Activates Lattice Oxygen in Perovskite Ferrite for Methane Partial Oxidation Coupled with CO_2-Splitting. *J. Am. Chem. Soc.* **2020**, *142*, 11540−11549.

(10) Kousi, K.; Neagu, D.; Bekris, L.; Papaioannou, E. I.; Metcalfe, I. S. Endogenous nanoparticles strain perovskite host lattice providing oxygen capacity and driving oxygen exchange and CH_4 conversion to syngas. *Angew. Chem., Int. Ed.* **2020**, *59*, 2510−2519.

(11) Quintella, S. A.; Saboya, R. M. A.; Salmin, D. C.; Novaes, D. S.; Araújo, A. S.; Albuquerque, M. C. G.; Cavalcante, C. L., Jr. Transesterificarion of soybean oil using ethanol and mesoporous silica catalyst. *Renewable Energy* **2012**, *38*, 136−140.

(12) Li, Y.; Zhou, G.; Li, C.; Qin, D.; Qiao, W.; Chu, B. Adsorption and catalytic activity of Porcine pancreatic lipase on rod-like SBA-15 mesoporous material. *Colloids Surf., A* **2009**, *341*, 79−85.

(13) Guan, M.; Liu, W.; Shao, Y.; Huang, H.; Zhang, H. Preparation, characterization and adsorption properties studies of 3-(methacryloy-loxy) propyltrimethoxysilane modified and polymerized sol−gel mesoporous SBA-15 silica molecular sieves. *Microporous Mesoporous Mater.* **2009**, *123*, 193−201.

(14) Salis, A.; Bhattacharyya, M. S.; Monduzzi, M. Specific ion effects on adsorption of lysozyme on functionalized SBA-15 mesoporous silica. *J. Phys. Chem. B* **2010**, *114*, 7996−8001.

(15) Katiyar, A.; Yadav, S.; Smirniotis, P. G.; Pinto, N. G. Synthesis of ordered large pore SBA-15 spherical particles for adsorption of biomolecules. *J. Chromatogr. A* **2006**, *1122*, 13−20.

(16) Lin, V. S.-Y.; Lai, C.-Y.; Huang, J.; Song, S.-A.; Xu, S. Molecular recognition inside of multifunctionalized mesoporous silicas: toward selective fluorescence detection of dopamine and glucosamine. *J. Am. Chem. Soc.* **2001**, *123*, 11510−11511.

(17) De Sousa, A.; Maria, D. A.; De Sousa, R. G.; De Sousa, E. M. B. Synthesis and characterization of mesoporous silica/poly (N-isopropylacrylamide) functional hybrid useful for drug delivery. *J. Mater. Sci.* **2010**, *45*, 1478−1486.

(18) Zhao, J.; Gao, F.; Fu, Y.; Jin, W.; Yang, P.; Zhao, D. Biomolecule separation using large pore mesoporous SBA-15 as a substrate in high performance liquid chromatography. *Chem. Commun.* **2002**, 752−753.

(19) Taguchi, A.; Schüth, F. Ordered mesoporous materials in catalysis. *Microporous Mesoporous Mater.* **2005**, *77*, 1−45.

(20) Liu, X.; Li, L.; Du, Y.; Guo, Z.; Ong, T. T.; Chen, Y.; Ng, S. C.; Yang, Y. Synthesis of large pore-diameter SBA-15 mesostructured spherical silica and its application in ultra-high-performance liquid chromatography. *J. Chromatogr. A* **2009**, *1216*, 7767−7773.

(21) Zhao, D.; Feng, J.; Huo, Q.; Melosh, N.; Fredrickson, G. H.; Chmelka, B. F.; Stucky, G. D. Triblock copolymer syntheses of mesoporous silica with periodic 50 to 300 angstrom pores. *Science* **1998**, *279*, 548−552.

(22) Sushkevich, V. L.; Palagin, D.; Ranocchiari, M.; van Bokhoven, J. A. Selective anaerobic oxidation of methane enables direct synthesis of methanol. *Science* **2017**, *356*, 523−527.

(23) Liu, Y.; Qin, L.; Cheng, Z.; Goetze, J. W.; Kong, F.; Fan, J. A.; Fan, L.-S. Near 100% CO selectivity in nanoscaled iron-based oxygen carriers for chemical looping methane partial oxidation. *Nat. Commun.* **2019**, *10*, 1−6.

(24) Ravikovitch, P. I.; Neimark, A. V. Characterization of micro-and mesoporosity in SBA-15 materials from adsorption data by the NLDFT method. *J. Phys. Chem. B* **2001**, *105*, 6817−6823.

(25) JuneáShin, H. Modification of SBA-15 pore connectivity by high-temperature calcination investigated by carbon inverse replication. *Chem. Commun.* **2001**, 349−350.

(26) Ryoo, R.; Ko, C. H.; Kruk, M.; Antochshuk, V.; Jaroniec, M. Block-copolymer-templated ordered mesoporous silica: array of uniform mesopores or mesopore− micropore network? *J. Phys. Chem. B* **2000**, *104*, 11465−11471.

(27) Plimpton, S. Fast parallel algorithms for short-range molecular dynamics. *J. Comput. Phys.* **1993**, *117*, 1−19.

(28) Hill, J.-R.; Sauer, J. Molecular mechanics potential for silica and zeolite catalysts based on ab initio calculations. 2. Aluminosilicates. *J. Phys. Chem. B* **1995**, *99*, 9536−9550.

(29) Hill, J. R.; Sauer, J. Molecular mechanics potential for silica and zeolite catalysts based on ab initio calculations. 1. Dense and microporous silica. *J. Phys. Chem. B* **1994**, *98*, 1238−1244.

(30) Mayo, S. L.; Olafson, B. D.; Goddard, W. A. DREIDING: a generic force field for molecular simulations. *J. Phys. Chem. B* **1990**, *94*, 8897−8909.

(31) Malek, K.; Coppens, M.-O. Effects of surface roughness on self-and transport diffusion in porous media in the Knudsen regime. *Phys. Rev. Lett.* **2001**, *87*, 125505.

(32) Shi, Y.; Lee, Y. T.; Kim, A. S. Knudsen diffusion through cylindrical tubes of varying radii: theory and Monte Carlo simulations. *Transp. Porous Media* **2012**, *93*, 517−541.

(33) Knudsen, M. Die Gesetze der Molekularströmung und der inneren Reibungsströmung der Gase durch Röhren. *Ann. Phys.* **1909**, *333*, 75−130.

(34) Guo, M.; Cheng, Z.; Liu, Y.; Qin, L.; Goetze, J.; Fan, J. A.; Fan, L.-S. Cobalt doping modification for enhanced methane conversion at low temperature in chemical looping reforming systems. *Catal. Today* **2019**, *350*, 156−164.